Earth Planet. Sci. Lett. 636 (2024) 118694

Contents lists available at ScienceDirect

Earth and Planetary Science Letters

journal homepage: www.elsevier.com/locate/epsl

Accessory mineral microstructure and chronology reveals no evidence for late heavy bombardment on the asteroid 4-Vesta

L.F. White [a,b,c,d,*], D.E. Moser [e], J.R. Darling [c], B.G. Rider-Stokes [d], B. Hyde [a,b,e], K.T. Tait [a,b], K. Chamberlain [f], A.K. Schmitt [g,h], J. Dunlop [c], M. Anand [d]

[a] Department of Natural History, Royal Ontario Museum, Toronto, Ontario, M5S 2C6, Canada
[b] Department of Earth Sciences, University of Toronto, Toronto, Ontario, M5S 3B1, Canada
[c] School of Earth and Environmental Science, University of Portsmouth, Portsmouth, PO1 3QL, UK
[d] School of Physical Sciences, The Open University, Milton Keynes MK7 6AA, UK
[e] Western University, London, Ontario, Canada N6A 3KL
[f] Department of Geology and Geophysics, University of Wyoming, 1000 E. University Ave, Laramie, Wyoming 82071-3006, USA
[g] Institute of Earth Sciences, Ruprecht-Karls-Universitat Heidelberg, Im Neuenheimer Feld 236, D-69120 Heidelberg, Germany
[h] John de Laeter Centre, Curtin University, Bentley. WA 6102, Australia

ARTICLE INFO

Keywords:
Apatite
EBSD
Eucrites
Late Heavy Bombrdment
U-Pb
Zircon

ABSTRACT

A long-standing paradigm in planetary science is that the inner Solar System experienced a period of intense and sustained bombardment between 4.2 and 3.9 Ga. Evidence of this period, termed the Late Heavy Bombardment is provided by the $^{40}Ar/^{39}Ar$ isotope systematics of returned Apollo samples, lunar meteorites, and asteroidal meteorites. However, it has been largely unsupported by more recent and robust isotopic age data, such as isotopic age data obtained using the U-Pb system. Here we conduct careful microstructural characterisation of baddeleyite, zircon, and apatite in six different eucrites prior to conducting SIMS and LA-ICP-MS measurement of U, Th, and Pb isotopic ratios and radiometric dating. Baddeleyite, displaying complex internal twinning linked to reversion from a high symmetry polymorph in two samples, records the formation of the parent body (4554 ± 3 Ma 2σ; n = 8), while structurally simple zircon records a tight spread of ages representing metamorphism between 4574 ± 14 Ma and 4487 ± 31 Ma (n = 6). Apatite, a more readily reset shock chronometer, records crystallisation ages of ~4509 Ma (n = 6), with structurally deformed grains (attributed to impact events) yielding U-Pb ages of 4228 Ma (n = 12). In concert, there is no evidence within the measured U-Pb systematics or microstructural record of the eucrites examined in this study to support a period of late heavy bombardment between 4.2 and 3.9 Ga.

1. Introduction

The Howardite-Eucrite-Diogenite (HED) clan of achondritic meteorites is believed to represent the asteroid 4-Vesta, with the eucrites sampling the basaltic crust of the differentiated planetesimal (Mittlefehldt, 2015). Crystallization ages for eucrites vary, with Hf-W ages of up to 35 Ma after calcium aluminium-rich inclusion (CAI) formation, highlighting protracted volcanism and metamorphism on the parent body (Touboul et al., 2015; Roszjar et al., 2016) following differentiation at 4565 Ma (Lugmair and Shukolyukov, 1998) and formation of the upper crust around 2.66 Myr after CAI formation (Hublet et al., 2017). Volcanism on 4-Vesta likely occurred very early in Solar System history (4567.2 ± 0.6 Ma; Misawa et al., 2005), producing the basaltic crust sampled by the eucritic meteorites. Basaltic flows likely cooled rapidly, with 5 m thick flows cooling to ambient conditions in less than a year (Yamaguchi et al., 1996). For deeper eucrites (< 12 km depth), this cooling rate slows to 1 ° / 10^4 years, approximately 11 million years to cool to ambient conditions (Miyamoto and Takeda, 1977). Following formation, models suggest that a relatively thin (< 25 km) crust would have led to thermal metamorphism of the basaltic eucrites at approximately 800 – 1000 °C (Yamaguchi et al., 2009). However, this is complicated by ongoing impact heating and reworking alongside thermal metamorphism (e.g. Yamaguchi et al., 1996). For equilibrated eucrites, homogenisation of pyroxene suggests metamorphic temperatures (c. 1000 °C) were retained for at least a million years (Yamaguchi et al., 1996), in agreement with the formation of metamorphic zircon (900 °C)

* Corresponding author.
E-mail address: lee.white@open.ac.uk (L.F. White).

https://doi.org/10.1016/j.epsl.2024.118694
Received 15 June 2023; Received in revised form 14 March 2024; Accepted 28 March 2024
Available online 16 April 2024

at 4554.5 ± 2 Ma (Iizuka et al., 2015).

Ancient and prolonged magmatism and metamorphism is also recorded within the eucrite accessory mineral record, with younger metamorphic events dated by zircon in eucrite meteorites Berba, Cachari, Caldera, Juvinas (weighted average $^{207}Pb/^{206}Pb$ age of 4550.21 ± 4.4 Ma ± 11 Ma; Zhou et al., 2013; Haba et al., 2019; Haba and Wotzlaw, 2021), Camel Donga (4552.56 ± 0.69 Ma; Haba and Wotzlaw, 2021), and Agoult (4554.5 ± 2 Ma; Iizuka et al., 2015), baddeleyite (monoclinic ZrO_2) in Alan Hills (ALHA) 80,103, ALHA 83,232 and EETA 81,006 (weighted average $^{207}Pb/^{206}Pb$ age of 4549 ± 18 Ma; Bukovanská et al., 1997), and apatite ($Ca_5(PO_4)_3(F,Cl,OH)$) in Agoult (model $^{207}Pb^*/^{206}Pb^*$ age of 4524.8 ± 9.6 Ma; Koike et al., 2020). Even younger ages are more challenging to interpret; for example, ^{182}Hf-^{182}W ages of 4532 ± (−11 / +6) Ma and 4565 ± 0.9 Ma of zircon in basaltic eucrites (Roszjar et al., 2016), 4531 ± 20 Ma zircon domains in Millbillillie (Hopkins et al., 2015) and 4517 ± 5 Ma apatite in Juvinas (Koike et al., 2020) could be dating either slow cooling of the crust or large impact events, leaving major uncertainties in the timing of parent body evolution.

Constraining the timing and severity of impact processes on 4-Vesta is particularly important given the role of the HED achondrites in establishing the hypothesis of late heavy bombardment (LHB) of the inner Solar System (Kring and Cohen, 2002). Originally defined by a preponderance of 3.9 billion-year-old ages measured in samples returned by the Apollo missions (Wetherill, 1975), the LHB could represent a short-lived, extreme influx of material at 3.9 Ga (Tera et al., 1974) or a prolonged period of bombardment generated through the tail end of planetary accretion (Morbidelli et al., 2012). $^{40}Ar/^{39}Ar$ systematics of eucrites record a preponderance of ages between 3.4 and 4.1 Ga (Marchi et al., 2013), with notable peaks at 3.5, 3.8, 3.9 and 4.0 Ga (Scott et al., 2009) which correlate with a comparable prevalence of 3.9 Ga ages which have been reported in the $^{40}Ar/^{39}Ar$ systematics of samples returned by the Apollo missions, as well as some lunar meteorites (Kring and Cohen, 2002). Younger impact events can also be identified within the $^{40}Ar/^{39}Ar$ systematics of eucrites, with NWA 1000 yielding an age of 646 ± 29 Ma which overprints an older 3922 ± 87 Ma age, which can be correlated with the proposed LHB (Takenouchi et al., 2021).

However, the natural evolution of $^{40}Ar/^{39}Ar$ systematics coupled with a gradual decrease in impact events linked to late accretion could also yield the distribution of Ar-Ar ages observed in Apollo samples (Boehnke and Harrison, 2016). In addition, studies examining the U-Th-Pb systematics coupled with the microstructure of accessory minerals such as zircon, baddeleyite, and apatite have revealed an absence of shock-reset ages and crystallographic features that could be confidently ascribed to this cataclysmic event in lunar and martian materials (Crow et al., 2017; Moser et al., 2019). Here, we analyse the microstructure and U-Th-Pb isotope systematics of these critical accessory mineral chronometers within six eucrites to provide new, empirical constraints on the timing, duration, and extent of magmatism and bombardment events on the asteroid 4-Vesta, most notably finding no evidence for an increased impact flux around 3.9 Ga, in agreement with recent studies on howardites (Cartwright et al., 2022)

1.1. Shock barometry and chronology of accessory minerals

Shock phenomena in zircon are well documented (Moser et al., 2011; Timms et al., 2017). At 20 GPa, the zircon lattice undergoes mechanical twinning (Morozova, 2015), while transformation to the high symmetry phase reidite occurs around 40 GPa (Leroux et al., 1999). Development of {110} shock twins has a minimal effect on the U-Pb systematics of the grain (Cavosie et al., 2018). However, local heating from a remnant impact melt sheet could encourage more complete age resetting (Moser et al., 2011). Though metastable over geological timelines, the reversion of reidite to zircon produces a range of granular neoblastic domains that preserve crystallographic evidence of the precursor phase (Cavosie et al., 2018). Within a melt sheet environment such as at the Vredefort impact structure, zircon can partially to fully recrystallize, forming neoblastic domains with U-Pb systematics reset to the timing of the impact event (Cavosie et al., 2015). At extreme temperatures (>2300 °C), zircon undergoes phase segregation to Si and Zr, forming a dissolution corona around the original grain (Timms et al., 2017). Despite the extreme temperatures affecting the rim of the grain, the isotope systematics of the zircon core remain undisturbed, retaining a concordant U-Pb age of protolith crystallization (Timms et al., 2017).

Baddeleyite undergoes a series of phase transformations under increasing pressure and temperature conditions. Above 3.5 GPa, the mineral transitions through a series of orthorhombic (I, II, III) structures (Kudoh et al., 1986), while high temperatures induce transformation to a tetragonal (> 1300 °C) or cubic (> 2300 °C) phase (Hannink et al., 2000). Though these high symmetry phases are metastable under ambient conditions, the formation and reversion of these phases result in unique crystallographic assemblages of daughter baddeleyite grains that can be reconstructed to reveal the parent phase (e.g. Cayron et al., 2006). In this way, reversion twinned baddeleyite can be utilized as a shock barometer, when reverted from the high-pressure orthorhombic phase (White et al., 2018), or as an indicator of high-temperature conditions when reverted from the tetragonal or cubic phases (e.g. Timms et al. 2017, White et al., 2020). These phase changes have extreme effects on the U-Th-Pb ages of individual domains. For example, baddeleyite grains in the lunar meteorite Northwest Africa (NWA) 3163, which contain microstructural domains formed by both igneous crystallization and high symmetry reversion, record ^{232}Th-^{208}Pb ages of 4.32 Ga and 2.17 Ga across a micrometre-scale distance (White et al., 2019). When rapidly quenched from a high symmetry polymorph full reversion does not occur, with the baddeleyite grain instead developing a quasi-amorphous texture and partially to fully losing radiogenic Pb through nanometre-scale grain boundaries and localised solid-state diffusion (Darling et al., 2016).

Apatite group minerals develop numerous microstructures at increasing shock pressures, including planar deformation features (> 10 GPa; Cavosie and Lugo Centeno, 2014; Slaby et al., 2017), crystal plastic deformation (Darling et al., 2020), fracturing and brecciation (Grange et al., 2013), and mosaicism and recrystallization (> 35 GPa; Schmieder et al., 2008; Slaby et al., 2017; Ćernok et al., 2019). The formation and evolution of these structures directly controls the chemical and volatile composition of the grain, affecting major element chemistry (Kenny et al., 2020) and isotopic compositions including Cl (Darling et al., 2020). Apatite is a more sensitive impact chronometer than baddeleyite or zircon, with a closure temperature to solid state Pb diffusion of between 375 - 600 °C (Cochrane et al., 2014; Schoene and Bowring, 2007). Pb diffusion and loss can be further enhanced by the microstructural complexity of the apatite grain, with shock deformation and recrystallization providing fast diffusion pathways that allow Pb isotopes to be used as a more effective impact recorder (e.g. McGregor et al., 2019).

In concert, the microstructural records of zircon, baddeleyite, and apatite provide unique insights into the conditions experienced by the host rock across a wide range of pressure and temperature regimes (e.g. Moser et al., 2011; Timms et al., 2017; Crow et al., 2017; White et al., 2018, 2020; Ćernok et al., 2019; Darling et al., 2020). By coupling quantified microstructural analysis with radiogenic age, the timing and severity of planetary processes can be measured empirically, yielding new insights into the formation and evolution of planetary bodies throughout the inner Solar System.

2. Materials and methods

2.1. Sample descriptions

In total, six unpaired eucrites have been incorporated into this study; NWA 1000, NWA 2202, and four that have not been examined since their initial classification (NWA 11,747, 11,748, 12,866, and 12,867).

Complete electron microprobe (EPMA) data, collected using a JEOL JXA8230 5-WDS electron probe microanalyzer (EPMA) instrument at the University of Toronto, for these samples can be found within the supplementary materials.

NWA 11,748 is a minimally brecciated monomictic eucrite consisting of subophitic clasts of gabbroic material set within a fine-grained matrix of the same materials (Gattacceca et al., 2020a). The main mass, totalling 27.5 g, displays a vesiculated fusion crust. Clinopyroxene ($En_{35}Fs_{58}Wo_7$; $n = 29$) displays exsolution lamella consistent with augite composition ($En_{30}Fs_{29}Wo_{41}$; $n = 5$), while all pyroxenes yield bulk Fe/Mn ratios of 31.49 ($n = 34$). Feldspar, where present, is unfractured and yields a tight spread of compositions around $An_{91} \pm 1.6\%$ 2σ ($n = 20$). Accessory minerals include ilmenite, troilite, apatite, merrillite, zircon, and rare baddeleyite.

NWA 11,747 is a highly brecciated monomictic eucrite consisting of highly fragmented medium-grained pyroxene and feldspar set within a fine-grained groundmass of the same minerals (Gattacceca et al., 2020a). The main mass (31.97 g) preserves a fusion crust, with a thin section of the sample revealing numerous dark grey to black melt glass pockets. Vesiculated melt veins crosscut the darker matrix of the stone. Pyroxene yields bulk Fe/Mn ratios of 29.42 ($n = 46$). Low calcium pyroxene ($En_{45}Fs_{46}Wo_8$; $n = 43$) dominates both domains with no observable chemical variation between the clasts and matrix. High-Ca lamella ($En_{35}Fs_{23}Wo_{42}$; $n = 3$) occur throughout the sample. Feldspar average An_{88} composition spread between An_{77} and An_{93} ($n = 25$). Apatite, merrillite, baddeleyite, and zircon occur as accessory phases.

NWA 1000 is a large (1.2 kg) unbrecciated eucrite comprising a subophitic and variolitic texture with laths of pyroxene (< 5 mm) and plagioclase (< 4 mm). Veins of fayalitic olivine crosscut the sample. Pyroxenes are zoned from $En_{68}Wo_4$ to $En_{16}Wo_{26}$ with minor chemical variation being introduced through an early reaction between pigeonite and the olivine veins ($En_{40}Wo_3$). A bulk Fe/Mn ratio of 38 supports classification as a eucrite. Roughly 50% of the feldspar ($An_{75–86}$) has been transformed to maskelynite (diaplectic feldspar glass) suggesting shock pressures in excess of around 17 GPa have been achieved at least locally within the sample (Hu et al., 2023). Silica is present in mesostasis regions, though has been altered by weathering that has also yielded carbonate veining within the sample. Accessory apatite, merrillite, zircon, and baddeleyite have been found within the sample. Two aliquots for $^{40}Ar/^{39}Ar$ analysis failed to yield an age plateau, though a cosmic ray exposure age of 30 ± 8 Ma was calculated (Kennedy et al., 2019). NWA 1000 yields Stannern-like geochemistry based on high Ti content (5.5 mg/g) and LREE/HREE enrichment with a negative Eu anomaly (Warren, 2002), making it geochemically unique within the scope of this study.

NWA 2202 is a polymict brecciated eucrite consisting of lithic and crystalline clasts (< 3 mm diameter) within a matrix of plagioclase and pyroxene. Accessory minerals include Fe-sulphide, chromite, ilmenite, baddeleyite, and zircon. Though plagioclase is crystalline, pyroxene displays planar deformation features and mottled extinction suggestive of low shock pressure deformation. Carbonate weathering veins to 0.1 mm width are common, lying alongside of and often completely enclosing the lithic clasts, separating them from the matrix. Ca-rich pyroxene ($Fs_{38.4 \pm 5.4}Wo_{28.4 \pm 5.8}$, $n = 19$; Fe/Mn = 32.4) and Ca-poor pyroxene ($Fs_{53.6 \pm 1.3}Wo_{6.7 \pm 2.2}$, $n = 6$; Fe/Mn = 30.8) are both present within the clasts and matrix, while feldspar in clasts ($An_{89.3 \pm 2.3}$, $n = 5$) and matrix ($An_{82.5 \pm 5.4}$, $n = 12$) yield statistically comparable anorthite numbers.

NWA 12,866, a single angular stone partially covered by a fusion crust, is a polymict breccia consisting of mineral clasts and rock fragments (< 2 cm) embedded within a fine-grained clastic matrix (Gattacceca et al., 2020b). Granular gabbroic rock fragments, composed of both pyroxene (ferrosilite ($Wo_{1.2–4.5}En_{32.1–42.7}$ $Fs_{55.9–66.5}$; Fe/Mn=29.9–32.5) with pigeonite lamellae ($Wo_{5.2–18.2}En_{32.3–41.5}Fs_{48.3–61.3}$; Fe/Mn=30.9–32.2), pigeonite ($Wo_{6.1–10}En_{27.1–32.4}Fs_{57.5–63.9}$; Fe/Mn=29.9–32.5) with augite lamellae ($Wo_{22.4–32.6}En_{27.8–37.3}Fs_{31.5–49.6}$;Fe/Mn=29.4–32.2) and plagioclase ($An_{72–90}$ with an average of An_{81}). Accessory minerals include ilmenite, chromite, tridymite and quartz (SiO_2), apatite, merrillite, zircon, and FeNi metal. Pyroxene minerals show no mosaicism, though augite lamella is locally displaced by low shock. Plagioclase is crystalline, with no evidence of maskelynite within the sample.

NWA 12,867, a polymict brecciated eucrite, is a small, rounded stone with a black fusion crust (Gattacceca et al., 2020b). The sample constitutes a mixture of mineral and basaltic clasts within a fine-grained clastic matrix. The largest lithological clast (ca. 60 mm) is a medium-grained enstatite-plagioclase rock with a granular texture hosting a large chromite grain. Pigeonite ($Wo_{5.1–17.1}En_{32.2–37.8}Fs_{45–59.4}$; Fe/Mn = 27.5–32) with augite lamellae ($Wo_{36.2–37.7}En_{26.9–34.5}Fs_{29.1–44.9}$; Fe/Mn =27.8–32.6) display no mosaicism or evidence of planar deformation features. Plagioclase ($An_{59–97}$ with an average of An_{87}) is unshocked in both clasts and matrix. Accessory phases include olivine ($Fo_{40.2–71.9}$ with an average of $Fo_{64.4}$), ilmenite, chromite, tridymite and quartz (SiO_2), apatite, merrillite, zircon and FeNi-metal.

2.2. Analytical methodology

Scanning electron microscopy (SEM) work was conducted on single thin sections of NWA 11,747, 11,748, 12,866 and 12,867, as well as 1-inch epoxy mounts of NWA 1000 and 2202, utilizing Energy-Dispersive X-ray spectroscopy (EDS) to identify P-rich grains and feature scan (automated, targeted EDS of grains using Z-contrast in backscatter electron imaging to identify phases of interest) to identify high contrast Zr phases. Instruments at the University of Portsmouth (Zeiss EVO 10MA LaB6 SEM) and the University of Western Ontario (Hitachi SU6600 VP-FEG SEM) were used to find and image grains, while Oxford Instruments Aztec software was used to reduce EDS data in all cases. High-resolution backscatter electron (BSE) imaging was conducted on grains of interest to identify internal fractures or inclusions. Zircon was located in all sections; apatite was located in five of the six samples (being absent only in NWA 2202) and baddeleyite was present in only four sections (absent in NWA 12,866 and 12,867).

2.2.1. Electron backscatter diffraction

Lattice orientation and internal microstructure of selected apatite, baddeleyite and zircon were studied by electron backscatter diffraction (EBSD). EBSD analyses were undertaken using an Oxford Instruments Nordlys-nano EBSD detector mounted on the same SEM at the University of Portsmouth, UK. Data were processed using Oxford Instruments Aztec software, and then further analysis of EBSD data was undertaken using the Channel 5 software suite. Diffracted electrons were collected at a tilt angle of 70°, using a primary electron beam with 20 kV accelerating voltage and 1 nA probe current in variable-pressure mode (N_2 was used to maintain chamber pressure of 20–30 Pa), broadly following the approach of Darling et al. (2016) and Ćernok et al. (2019). Diffraction patterns were automatically captured and indexed every 50–500 nm across manually defined areas. Apatite diffraction patterns were indexed to the chlorapatite crystal lattice parameters of Hughes et al., 1989. Baddeleyite was indexed against inorganic crystal structure database (ICSD) card 15,983 (Smith and Newkirk, 1965). Wild spike reduction was conducted on all datasets, though no other form of raw data correction was undertaken.

2.2.2. Geochronology

For baddeleyite and zircon, secondary ionization mass spectrometry (SIMS) was utilized to measure U-Pb geochronology, while laser ablation inductively coupled plasma mass spectrometry (LA-ICP-MS) was used to date individual apatites. Reconnaissance imaging of the target grains using SEM was conducted prior to analysis to avoid surficial cracks and fractures in zircon and baddeleyite, while EBSD allowed targeted dating of crystallographic regions of apatite in all studied samples.

SIMS analysis of U-Pb systematics was conducted on fifteen grains in total across NWA 1000 and NWA 2202 (eight baddeleyite and seven zircon) following previously reported procedures described in Schmitt et al. (2010) using a CAMECA ims 1270 ion microprobe housed at UCLA. An aperture-delimited primary beam of ~8 nA 16O- was focused onto a ~20 μm diameter spot. Lateral resolution was enhanced by narrowing the field aperture to an effective sampling area of 10 × 10 μm which was irradiated into the analyzed zircon or baddeleyite grain. Relative sensitivity factors for U-Pb in baddeleyite and zircon were calibrated on Phalaborwa baddeleyite and AS3 zircon references (Heaman, 2009; Paces and Miller, 1993).

LA-ICP-MS analysis of U-Pb apatite grains within NWA 11,747, 11,748, 12,866 and 12,867 was undertaken at the University of Portsmouth. For all grains, correlative EBSD was conducted prior to LA-ICP-MS analyses, which utilised an ASI RESOlution 193 nm ArF excimer laser coupled to an Analytik Jena Plasma Quant Elite ICP MS. Single spot ablations were conducted using either a 30 μm, 25 μm or 15 μm spot size (based on available phosphate surface area) and operating the laser at 3 Hz and 2.5 J/cm^{-2}, during a 30-second ablation. MAD apatite (Thomson et al. 2012) was used as the primary reference material to correct for mass bias, instrument drift, and laser-induced elemental fractionation, with a ^{207}Pb/^{206}Pb based common-Pb correction scheme to the primary reference material following Chew et al. (2014). The accuracy and precision of analyses were monitored using Xuxa apatite (573.0 ± 0.8 Ma; Schuch 2018), and McClure Mountain apatite (523.98 ± 0.12 Ma; Schoene and Bowring 2006). The results for unconstrained Tera-Wasserburg Concordia regressions for each reference material are within the uncertainty of reference U-Pb ages and common ^{207}Pb/^{206}Pb values.

3. Results

3.1. Accessory mineral occurrence and textures

A feature scan of NWA 11,747 revealed 54 baddeleyite grains (8.8 μm^2–137.6 μm^2 exposed surface area) and 404 zircons (8.8 μm^2–2114 μm^2). Zircon grains display a range of morphologies, predominately occurring as either small, rounded grains (Fig. 1a, b) or as conglomerates of granoblastic grains (Fig. 1c, d). Baddeleyite occurs as exceptionally small grains throughout the sample (< 10 μm), rarely with small fractures cross-cutting individual crystals (Fig. 1e, f). Elemental mapping of the thin section revealed two large (> 500 μm^2) calcium phosphate grains within gabbroic clasts, though smaller apatite and merrillite grains were present throughout the groundmass. Grains are highly fractured, though appear homogenous in BSE and EDS.

A high-resolution feature scan of NWA 11,748 revealed 3 baddeleyite grains (21.7–205 μm^2) and 264 zircon grains (8.8 μm^2–817 μm^2). Zircon occurs as small, rounded grains throughout the thin section (Fig. 1f-j), with one of the nine grains imaged displaying minor fracturing. Baddeleyite is incredibly rare, occurring as clusters of small grains within pockets of amorphous silica (Fig. 1k,l). Mapping of the section using EDS reveals an abundance of phosphate grains across the sample, primarily occurring in the brecciated matrix. Individual grains range from 5 μm to > 400 μm in length and appear largely free of fractures and inclusions in BSE imaging.

Four zircon grains (< 1 to 25 μm) were found in a scan of NWA 12,866, occurring with silica and ilmenite within both clasts and matrix of the thin section. Zircon within the matrix are small, rounded, anhedral grains, while those within clasts are polycrystalline (granular) aggregates of small zircon neoblasts. Baddeleyite was not found in the sample. Elemental mapping of NWA 12,866 reveals multiple apatite and merrillite grains within the sample, varying in size from 20 to 120 μm. Grains are highly fractured and contain up to three unique orientations of planar deformation features. Some grains are crosscut by melt veins, though otherwise appear homogenous in BSE imaging.

NWA 12,867 contains a single zircon grain (40 μm) and no baddeleyite. The zircon grain is anhedral, occurring as an irregularly shaped elongate bleb intergrown with apatite. Phosphate minerals (< 200 μm), however, were located within both the clast and matrix of the sample. Apatite and merrillite are crosscut by irregular cracks and fractures, though appear otherwise homogenous in BSE.

3.2. Quantification of microstructure using electron backscatter diffraction (EBSD)

Zircon grains in NWA 1000, 2202, 11,747, and 11,748 are microstructurally simple, displaying < 2° of total misorientation across a single crystallographic orientation (Fig. 2a-c) and igneous zoning in

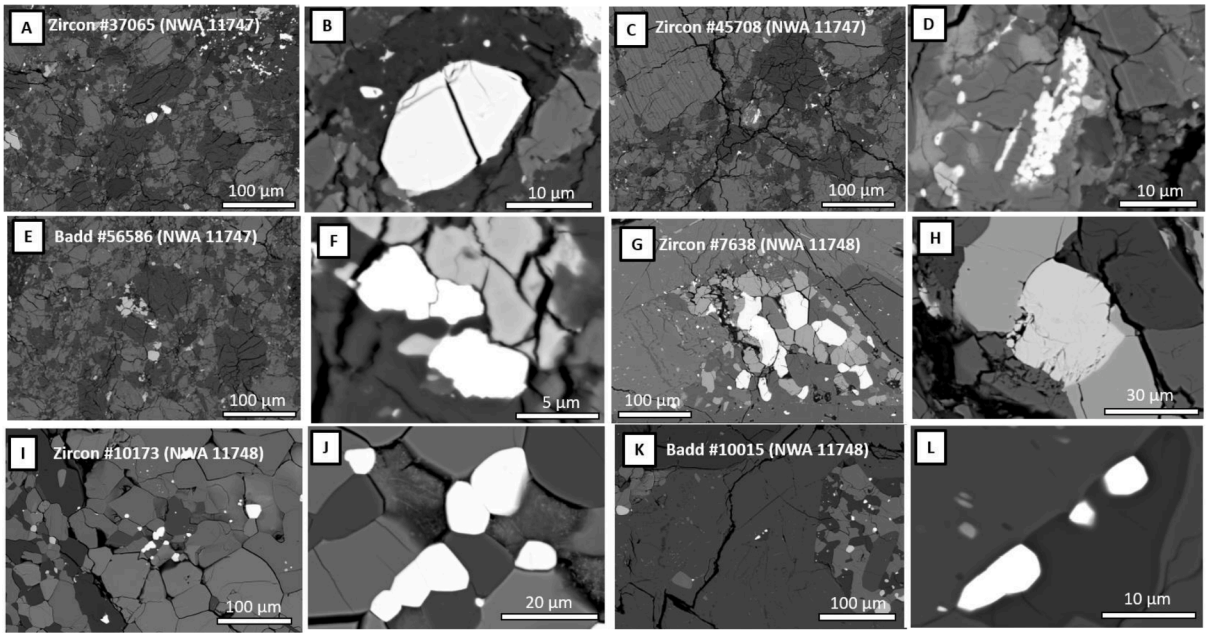

Fig. 1. Backscatter electron (BSE) imaging of zircon (**A-D**) and baddeleyite (**E,F**) in NWA 11,747, and zircon (**G-J**) and baddeleyite (**K,L**) in NWA 11,748, to highlight the range of grain morphologies observed in the analysed eucrites. Lighter grey minerals are pyroxene, while darker grey crystals are feldspar (plagioclase).

cathodoluminescence (CL; Fig. 2d). Within NWA 12,866, granular zircon records a range of unique crystallographic orientations, with high-angle grain boundaries dividing the sub grains (Fig. 2e). EBSD analysis of baddeleyite grains within NWA 11,748 reveals complex, irregular, micrometre- to submicrometre-scale baddeleyite domains divided by sub-grain boundaries that yield weaker electron diffraction patterns. Crystalline subdomains yield distinct, loosely clustered, orthogonally related groups of crystallographic orientations in <100>, ⟨010⟩, and ⟨001⟩ pole figures (Fig. 3). A range of unique disorientation relationships between the domains, predominately 90°/<001>, 180°/<001>, and 180°/<9,0,10>, can be measured in each grain.

Apatite reveals a range of structures across the five samples analysed, including widespread evidence for plastic deformation, amorphization, fracturing, and local recrystallization (Fig. 4). Two eucrites (NWA 11,748 and 12,867) contain minimally deformed apatite that displays < 10° cumulative misorientation across the length of each crystal. Whereas three eucrites (NWA 1000, 11,747, and 12,866) host highly deformed grains with between 30 and 50° of cumulative misorientation, with NWA 11,747 displaying grains of randomly oriented neoblasts in close association with the grain. Within NWA 1000, small regions of apatite fail to diffract, suggesting amorphization of the crystal structure on the length scale of EBSD (c. 50 nm).

3.3. Geochronology

SIMS analysis of baddeleyite within NWA 1000 reveals two age populations: ancient ^{207}Pb-^{206}Pb ages with a weighted average age of 4558 ± 5 Ma (2σ; n = 6) and two younger grains yielding ages of 4478 ± 20 Ma and 4457 ± 15.4 Ma (weighted average of 4464.8 ± 11.9 Ma). Two baddeleyite grains in NWA 2202 give ages of 4563 ± 18 Ma and 4527 ± 33 Ma. Data are reversely discordant (likely from recent Pb loss through fast diffusion along microstructural pathways; Pohlner et al., 2020), and therefore only ^{207}Pb-^{206}Pb ages are considered. Zircon grains yield concordant SIMS ages, with a single zircon grain in NWA 1000 recording a ^{207}Pb-^{206}Pb age of 4510 ± 17 Ma, while zircon in NWA 2202 displays a spread of ages between 4574 ± 15.5 Ma and 4511 ± 8.9 Ma (with a weighted average of 4542 ± 8 Ma, MSWD = 4). All zircon and baddeleyite analyses contained very low common Pb (> 99.1% radiogenic ^{207}Pb) and are summarised in Table 1.

LA-ICP-MS analysis of apatite within NWA 1000 reveals concordant U-Pb systematics (^{206}Pb/^{238}U vs. ^{207}Pb/^{235}U concordia age of 4498.7 ± 6.2 Ma) with a weighted average ^{207}Pb/^{206}Pb age of 4486 ± 18 Ma (n = 3). NWA 11,748 records slightly discordant U-Pb age systematics, with an upper intercept age of 4527 ± 41 Ma. A weighted average ^{207}Pb/^{206}Pb age of 4512 ± 4.9 Ma (n = 4) supports this ancient upper intercept age. NWA 12,867 yields discordant U/Pb ages, with a weighted average of ^{207}Pb/^{206}Pb age of 4509 ± 34 Ma (n = 4). NWA 11,747 apatite records a spread of ^{207}Pb/^{206}Pb ages between 4242 ± 12 Ma and 4171 ± 16 Ma, yielding an upper intercept concordia age of 4193 ± 320 Ma (n = 4), while NWA 12,866 records ^{207}Pb/^{206}Pb ages between 4268 Ma and 4190 Ma (n = 8), 62% of which are concordant. All apatite LA-ICP-MS data are reported in the supplementary data tables and summarised in Table 1 and Fig. 5.

4. Discussion

4.1. Magmatism and cooling on the eucrite parent body

Structurally complex baddeleyite grains are observed here in NWA 11,748, which contain evidence for reversion twinning indicative of a precursor high temperature (> 1300 °C) or pressure (> 5 GPa) polymorph (White et al., 2018 & 2020). These structures are unlikely to be produced through igneous processes alone, as baddeleyite (monoclinic-ZrO_2) would crystallize directly from the melt either untwined or with simple 180°/<001> twin relationships (White et al., 2018). As such, baddeleyite grains must have formed prior to exposure to the high pressure or temperature event which facilitated transformation to the high symmetry zirconia polymorph, and as such baddeleyite could preserve evidence for the earliest accretion and differentiation processes on the eucrite parent body. In concert, baddeleyite in NWA 1000 and NWA 2202 preserve the oldest measured U-Pb ages (c. 4558 Ma) within the six samples studied, supportive of eucrite formation within the first few million years of Solar System history (e.g. Hopkins et al., 2015; Hublet et al., 2017).

The youngest baddeleyite age in NWA 1000 (4457 ± 15.4 Ma) likely reflects either continued global thermal metamorphism on the eucrite parent body or impact-induced Pb diffusion and age resetting (Jourdan et al., 2020). The extensive crystal plastic deformation observed in

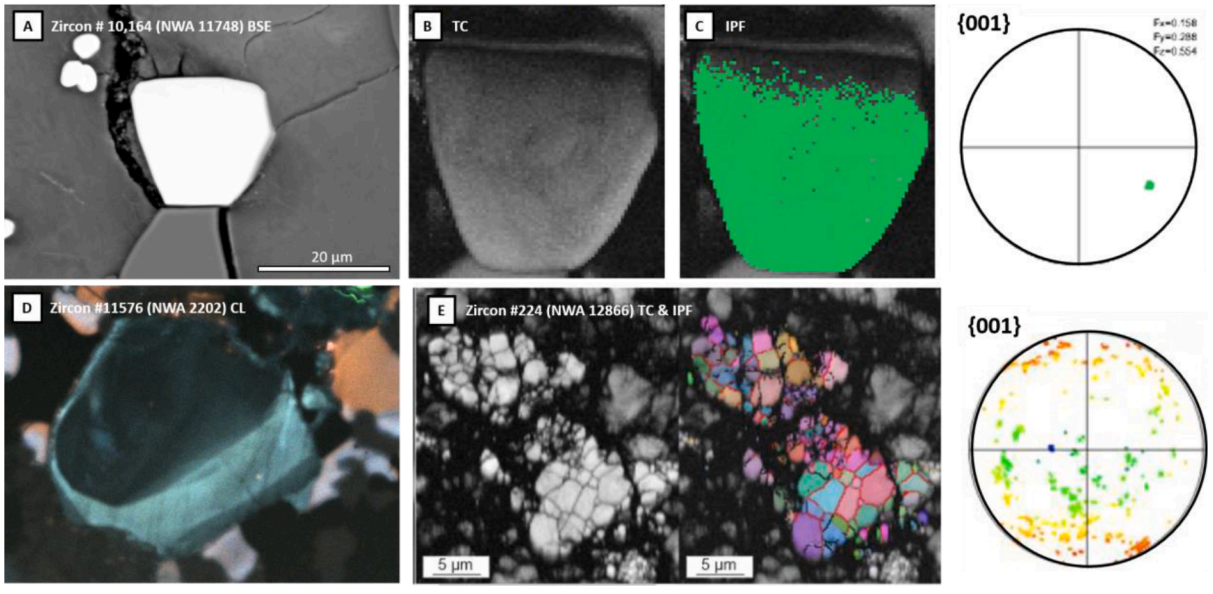

Fig. 2. Backscatter electron (BSE) imaging of zircon grain #10,164 in NWA 11,748 (**A**). A texture component (TC) map of the grain reveals no internal metamictization (**B**), while an inverse pole figure (IPF) map reveals the uniform structure of the grain (**C**). Cathodoluminescence imaging (CL) of zircon grain #11,576 in NWA 2202 reveals igneous zonation (**D**). Two zircon grains in NWA 12,866 are comprised of randomly oriented clusters of individual sub-micrometre neoblasts are revealed by both TC and IPF maps of the grains (**E**).

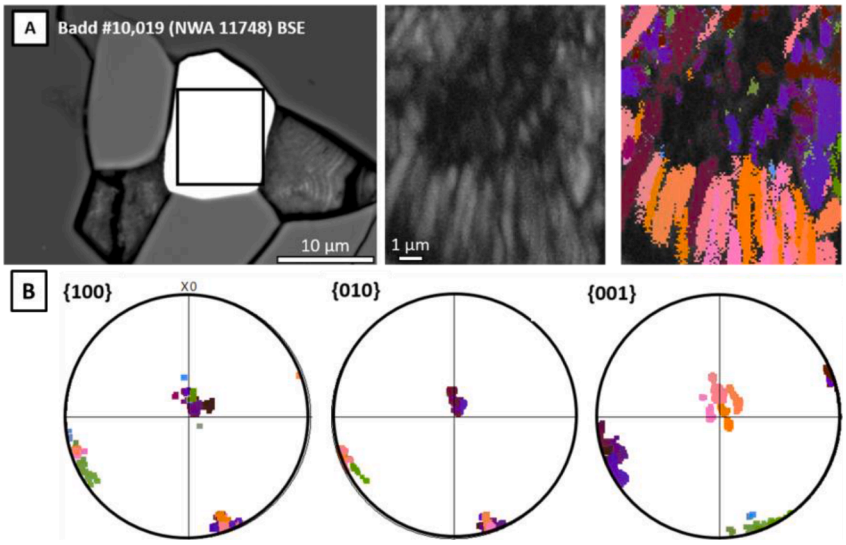

Fig. 3. Electon Backscatter Diffraction (EBSD) data for baddeleyite in NWA 11,748. Grains occur in association with amorphous silica (**A**), are variably diffracting in band contrast imaging, and display complex orthorhombic relationships (90°) between twin domains. Crosses in {100}, {010} and {001} inverse pole figures (**B**), offset by 90°, are indicative of the former presence of a high symmetry, high pressure-temperature zirconia polymorph (e.g. White et al., 2020).

apatite in NWA 1000, which appears slightly older (4486 ± 18 Ma) than two of the baddeleyite grains, suggests an impact event around 4460 Ma which reset, or partially reset, the Pb isotope systematics of apatite and baddeleyite within the sample.

The suite of zircon analysed in this study, despite containing no evidence for shock annealing or deformation, records a spread of ages between baddeleyite crystallization (4557 Ma) and 4487 ± 31.2 Ma in NWA 2202. Though comparable young ages in eucritic zircon (e.g. 4530 Ma) have previously been attributed to impact resetting (Hopkins et al., 2015), the absence of microstructural features associated with impact-induced Pb loss (such as {112} micro twin lamella or granoblastic textures) suggests an endogenic origin for the grains. Eucritic zircon could also be formed during burial metamorphism, whereby partial melting of silica-rich mesostasis and ilmenite ($FeTiO_3$) leads to a reaction between Si and Zr (Haba et al., 2014; Iizuka et al., 2015). Theoretically, heating from an impact-induced melt sheet could produce a similar temperature regime (900 – 1000 °C) in underlying target rocks, resulting in fresh zircon growth. However, baddeleyite grains in NWA 2202 yield ^{207}Pb-^{206}Pb ages of 4563 ± 18 Ma and 4527 ± 33 Ma, predating zircon formation. Baddeleyite would undergo a phase transition to the high-symmetry tetragonal polymorph (t-ZrO_2) at these pressure-temperature conditions (Timms et al., 2017), before producing an array of reversion microstructures during the transition back to the ambient monoclinic structure (White et al., 2018). These structures act as low-temperature diffusion pathways for Pb loss, and as such the retention of ancient ^{207}Pb-^{206}Pb ages suggests no exposure to metamorphic or annealing conditions. As such, we move forward on the assumption that the spread of zircon ages in NWA 2202 can be attributed to endogenic mechanisms.

The spread of ages preserved within the clasts and matrix of brecciated eucrite NWA 2202 are thus attributed to thermal alteration on 4-Vesta until at least 4487 Ma, falling outside of young zircon ages (> 4532 Ma) supportive of prolonged Vestan magmatism (Roszjar et al., 2016). Given the brecciated nature of the sample, the stratigraphic depth of formation for these clasts is poorly constrained, though the younger ages suggest formation at depth on the parent body (potentially up to 20 km deep) prior to excavation and brecciation (e.g. Iizuka et al., 2019). This interpretation is further supported by U-Pb analysis of minimally deformed apatite grains in NWA 1000, NWA 11,748 and NWA 12,867, which all preserve ages around ~4500 Ma that are likely attributed to cooling of the parent body. These microstructurally constrained ages are supported by high precision isotope dilution thermal ionisation mass spectrometry (ID-TIMS) zircon ages from Camel Donga of 4552.56 ± 0.69 Ma (Haba and Wotzlaw, 2021) and Agoult of 4554.5 ± 2 Ma (Iizuka et al., 2015), as well as $^{40}Ar/^{39}Ar$ ages from cumulate eucrites Moore County and Moama (> 4531 ± 11 Ma; Jourdan et al., 2020). Our data thus provide further support for early global metamorphism on the eucrite parent body (Iizuka et al., 2015; Haba and Wotzlaw, 2021), potentially driven by sustained magmatism (Roszjar et al., 2016) and prolonged cooling of the eucrite source through insulating crustal layers (4514 ± 6 Ma; Jourdan et al., 2020).

Previous $^{40}Ar/^{39}Ar$ data from three polymict eucrites, which yielded apparent age plateaus of between 4543 ± 56 Ma and 4491 ± 16 Ma, were ascribed to widespread resetting during an impact event at 4500 ± 4 Ma (Kennedy et al., 2019). However, the absence of any structural or isotopic evidence for this event in the six eucrites studied here suggests that any impact at this time would have to be small and localized and is unlikely to represent a significant resetting event on the eucrite parent body (Fig. 6). The absence of clear impact resetting at 4500 Ma in the $^{40}Ar/^{39}Ar$ systematics of howardites NWA 1929 and Dho 485 further supports this interpretation (Cartwright et al., 2022).

4.2. Timing and severity of bombardment events recorded by eucrites

Given the highly brecciated nature of five of the six studied eucrites (NWA 2202, NWA 11,747, NWA 11,748, NWA 12,866, and NWA 12,867), and the polymict nature of three (NWA 2202, NWA 12,866, and NWA 12,867), the analysed samples were exposed to impact gardening and reprocessing within an array of geological terranes on the surface of the eucrite parent body (e.g. Kennedy et al., 2019; Jourdan et al., 2024). The absence of shock features in the ancient baddeleyite and zircon examined here suggests that large early impact events, such as the mesosiderite-forming hit-and-run event at 4525.39 ± 0.85 Ma (Haba et al., 2019) or remnant impactors from the moon forming impact at around 4470 Ma (Bottke et al., 2015), were not recorded in a globally diverse range of eucrites. Interestingly, the sampled eucrites also do not record isotopic evidence for either the Rheasilvia (3.5 ± 0.1 Ga) or Veneneia (3.7 ± 0.1 Ga) crater-forming impact events (Schmedemann et al., 2014), though these ages are generally under-represented for eucrites as a whole (including in ^{40}Ar-^{39}Ar age systematics; Jourdan et al., 2024).

Extensively deformed and recrystallized apatite grains within NWA

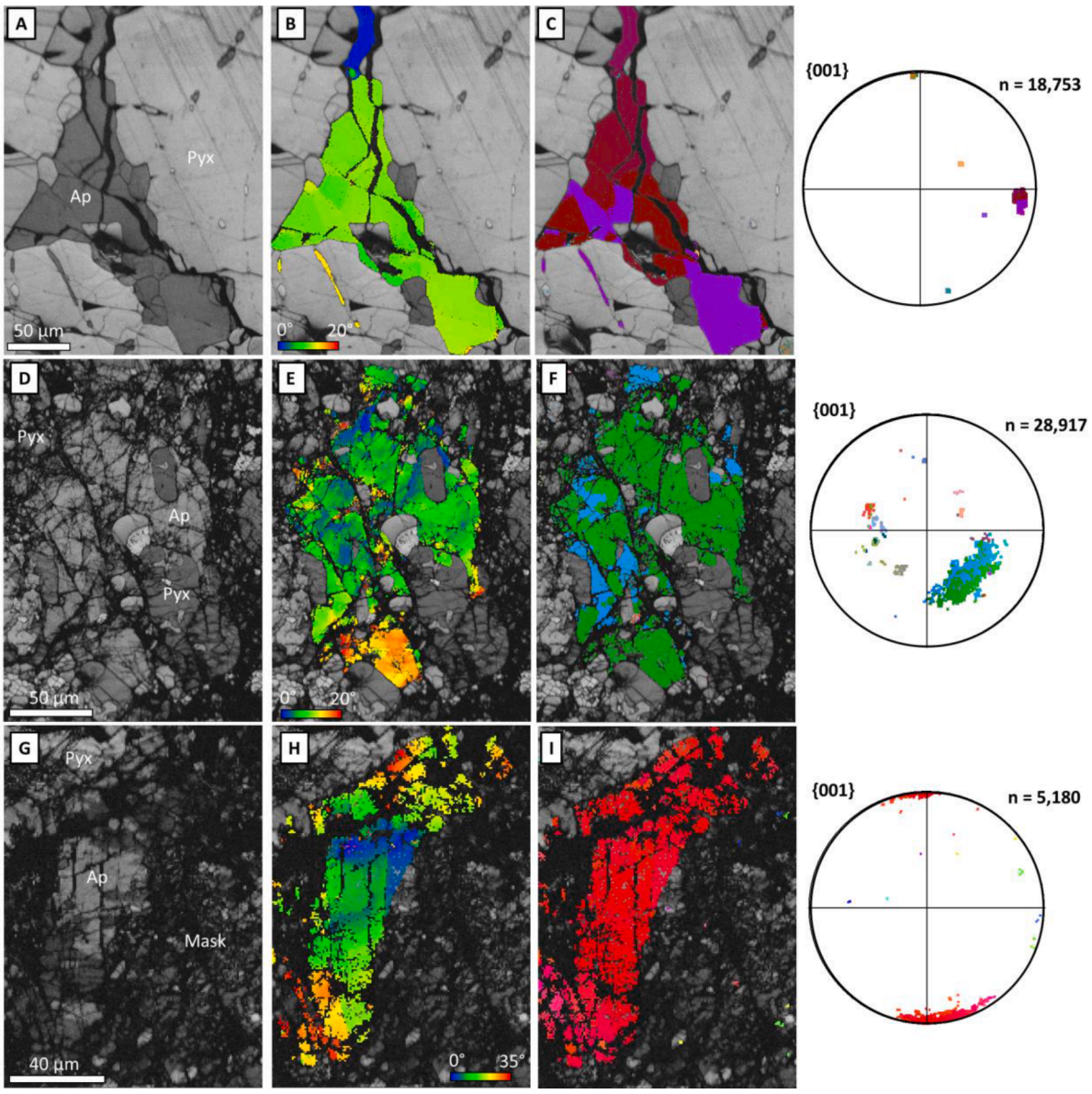

Fig. 4. EBSD of apatite grains in three of the eucrites studied (NWA 11,747, 11,748 and 1000). Phosphate minerals could not be located in NWA 2202. Apatite in NWA 11,748 are highly crystalline (**A**), displaying minimal crystal plastic deformation (**B**) and minimal spread of orientations in inverse pole figure (IPF) colouring (**C**). Apatite in NWA 11,747 appears more damaged, with inclusions and open fractures cross cutting the grain (**D**). Grains are deformed, hosting up to 18° of internal crystal plastic deformation (**E**) and a large spread of similar orientations in IPF (**F**). Apatite in NWA 1000 also appear fractured and are surrounded by poorly diffracting domains of maskelynite (**G**). Grains are deformed by up to 35° of internal crystal plastic deformation (H), resulting in a wide spread of orientations in IPF maps and pole figures, which also displays the number of individual pixels (n) measured by EBSD and incorporated into the maps (**I**).

11,747 and NWA 12,866 record ^{207}Pb-^{206}Pb ages of between 4269 ± 13 Ma and 4171 ± 16 Ma. Correlating microstructure (EBSD) and U-Pb age dating (LA-ICP-MS) of apatite grains is highly suggestive of impact-induced Pb loss and age resetting, revealing at least one significant impact event on the asteroid 4-Vesta around 4170 Ma. Given the sensitivity of apatite to age resetting, whereby grains start to lose Pb through solid-state diffusion at < 570 °C (significantly lower than baddeleyite and zircon (900 °C); Cherniak, 2010), it is significant that the highly deformed grains within our analysed population still preserve U-Pb ages older than peak LHB at 4.1 Ga (Nemchin et al., 2009). Assuming the inner Solar System was exposed to both more frequent and more severe impact events during a period of late heavy bombardment (e.g. Kring and Cohen, 2002), it is expected that at least some of the accessory minerals analysed within these six eucrites would preserve isotopic or structural evidence of the event given the expected wide-spread generation of highly heated materials (Marchi et al., 2013). For example, it has previously been shown that the boundary domains in reversion twinned baddeleyite are highly sensitive to Pb loss during low temperature (greenschist-facies; < 450 °C) metamorphic events (White et al., 2017). However, despite showing comparable microstructures, the grain population analysed here displays no evidence for Pb loss at any point following crystallization c. 4558 Ma ago. A large impact event could also be recorded by merrillite in the Juvinas meteorite (4150.3 ± 10.4 Ma) and apatite in the Stannern meteorite (4143.0 ± 12.5 Ma)

Table 1
A summary of all U-Pb analyses on eucrites reported in this study. For each sample, a selection of characterised baddeleyite (Badd.), zircon and apatite grains were measured to constrain the crystallization or impact age of the sample. Full data tables, including values obtained on reference materials, can be found in the supplementary data tables.

Sample	Mineral	$^{207}Pb/^{206}Pb$ Age (Ma)	2σ	$^{206}Pb/^{238}U$	2σ	$^{207}Pb/^{235}U$	2σ	$^{207}Pb/^{206}Pb$	2σ
NWA 1000	Badd.	4547	15.7	1.289	0.107	109.600	4.600	0.616	0.007
	Badd.	4562	8.62	1.420	0.091	121.900	3.930	0.623	0.004
	Badd.	4555	11.2	1.195	0.107	102.100	4.550	0.620	0.005
	Badd.	4561	3.66	1.385	0.110	118.800	4.710	0.622	0.002
	Badd.	4557	5.66	1.562	0.113	133.700	4.860	0.621	0.002
	Badd.	4547	9.14	1.523	0.096	129.400	4.090	0.617	0.004
	Badd.	4478	20	1.687	0.123	136.700	4.850	0.588	0.008
	Badd.	4457	15.36	1.797	0.106	143.500	4.260	0.579	0.006
	Zircon	4510	17.16	1.046	0.056	86.680	2.340	0.601	0.007
	Apatite	4491.4	15.6	1.040	0.036	86.01	2.19	0.593	0.006
	Apatite	4494.9	17.5	1.002	0.035	82.30	1.96	0.595	0.007
	Apatite	4474.4	15.0	1.020	0.035	81.91	1.94	0.586	0.006
NWA2202	Badd.	4563	18.22	1.147	0.068	98.520	2.970	0.623	0.008
	Badd.	4527	33.2	1.160	0.101	97.230	4.370	0.608	0.014
	Zircon	4574	15.52	1.037	0.068	89.810	2.940	0.628	0.007
	Zircon	4555	10.88	1.081	0.076	92.330	3.260	0.620	0.005
	Zircon	4527	33.2	0.965	0.079	80.930	3.430	0.608	0.014
	Zircon	4487	31.2	1.059	0.177	86.380	6.870	0.591	0.013
	Zircon	4554	7.2	1.060	0.065	90.520	2.780	0.619	0.003
	Zircon	4541	8.82	1.064	0.065	90.070	2.770	0.614	0.004
	Zircon	4511	8.94	1.008	0.048	83.590	1.990	0.601	0.004
NWA 11,748	Apatite	4514.0	23.1	0.957	0.029	82.00	1.21	0.603	0.010
	Apatite	4513.3	8.5	0.935	0.026	77.56	0.41	0.602	0.004
	Apatite	4513.8	9.5	0.952	0.028	78.98	0.42	0.602	0.004
	Apatite	4509.7	8.5	1.021	0.030	84.22	0.51	0.601	0.004
NWA 11,747_1	Apatite	4242.4	12.3	0.950	0.028	65.82	0.48	0.500	0.004
	Apatite	4188.9	23.3	0.955	0.030	64.82	0.74	0.483	0.008
	Apatite	4171.4	16.4	0.966	0.029	62.63	0.67	0.477	0.005
	Apatite	4203.9	21.0	0.891	0.028	60.67	0.87	0.488	0.007
NWA 12,866_1	Apatite	4190.5	16.5	0.961	0.030	63.91	2.02	0.483	0.005
	Apatite	4220.4	9.9	0.891	0.026	60.50	1.81	0.493	0.003
	Apatite	4232.3	8.8	0.908	0.027	62.16	1.86	0.497	0.003
	Apatite	4203.9	29.0	0.871	0.029	58.58	2.10	0.488	0.010
	Apatite	4247.1	16.1	0.902	0.028	62.33	1.93	0.502	0.006
	Apatite	4240.6	9.4	0.909	0.027	62.65	1.89	0.500	0.003
	Apatite	4269.5	13.0	0.936	0.029	65.78	2.08	0.510	0.005
	Apatite	4229.5	18.3	1.073	0.037	68.11	2.38	0.496	0.006
NWA 12,867_1	Apatite	4370.2	193.6	0.885	0.080	83.71	9.45	0.546	0.072
	Apatite	4360.0	181.0	0.817	0.078	74.02	7.27	0.542	0.067
	Apatite	4520.3	37.2	1.829	0.119	148.07	8.93	0.605	0.016
	Apatite	4511.4	165.9	0.860	0.067	86.60	8.27	0.601	0.069

(Koike et al., 2020); while this could reconcile the younger apatite ages reported here (4190 Ma in NWA 12,866), structural or isotopic evidence of the event is again absent in the ancient baddeleyite and zircon crystallographic record.

In total, 32 unique U-Th-Pb analyses of baddeleyite, zircon, and apatite reveal new insights into the formation and evolution of the eucrite parent body (4-Vesta). Ages of reversion twinned baddeleyite in the samples studied here support early magmatism on the parent body around 4558 Ma, in close agreement with previous studies (e.g. 4560 Ma baddeleyite in Juvinas; Bukovanská et al., 1997). Structurally simple zircon grains record ages between crustal formation and 4487 ± 31.2 Ma, which likely records a significant metamorphic event on 4-Vesta. The six eucrites analysed contain no geochronological evidence for a hypothesized period of late heavy bombardment, making our results consistent with those from accessory minerals on the Moon (Crow et al., 2017) and Mars (Moser et al., 2019), as well as studies of howardites (Cartwright et al., 2022) and diogenites (Jourdan et al., 2024). This conclusion is supported by the microstructural state of the analysed minerals, which fail to record indicative evidence of shock deformation beyond crystal plastic deformation within > 4.1 Ga apatite. This study also highlights the potential of apatite as a shock chronometer (e.g. Ćernok et al., 2019), whereby the correlated analysis of microstructure and U-Pb isotopes facilitates significantly enhanced interpretation of generated age data, here placing new constraints on the evolution of the asteroid 4-Vesta.

5. Conclusions

This study combined measurements of quantified microstructure and U-Th-Pb isotope systematics in apatite, baddeleyite, and zircon to yield empirical new insights into the formation and evolution of 4-Vesta. Baddeleyite grains, which contain crystallographic evidence for the former presence of a high symmetry precursor phase (White et al., 2018 & 2020), yield U-Pb ages of 4558 Ma, in agreement with the age of crustal formation on 4-Vesta (4561 Ma; Hopkins et al., 2015; Hublet et al., 2017). Granular zircon grains in NWA 12,866 are suggestive of a large impact event around 4.23 Ga, based on apatite Pb-Pb chronology from the same sample. Zircon grains in NWA 1000 and NWA 2202 yield Pb-Pb ages suggestive of prolonged crustal metamorphism between 4557 and 4510 Ma, while structural characterisation of these grain populations rule out impact resetting of the measured U-Pb systematics. In concert, these analyses provide no structural or isotopic evidence for

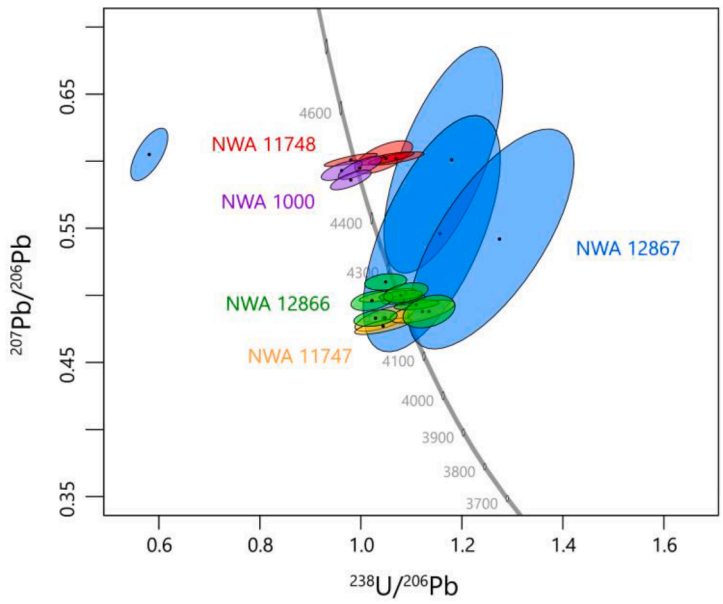

Fig. 5. Tera-Wasserberg diagram ($^{207}Pb/^{206}Pb$ vs. $^{238}U/^{206}Pb$) summarising LA-ICP-MS U-Pb measurements of apatite in NWA 1000 ($n = 3$), NWA 11,747 ($N = 4$), NWA 11,748 ($n = 4$), NWA 12,866 ($n = 8$) and NWA 12,867 ($n = 4$). Apatite in NWA 12,867 display high degrees of crystal plastic deformation, which would allow for significant Pb mobility and loss. Concordia tick marks in Ma.

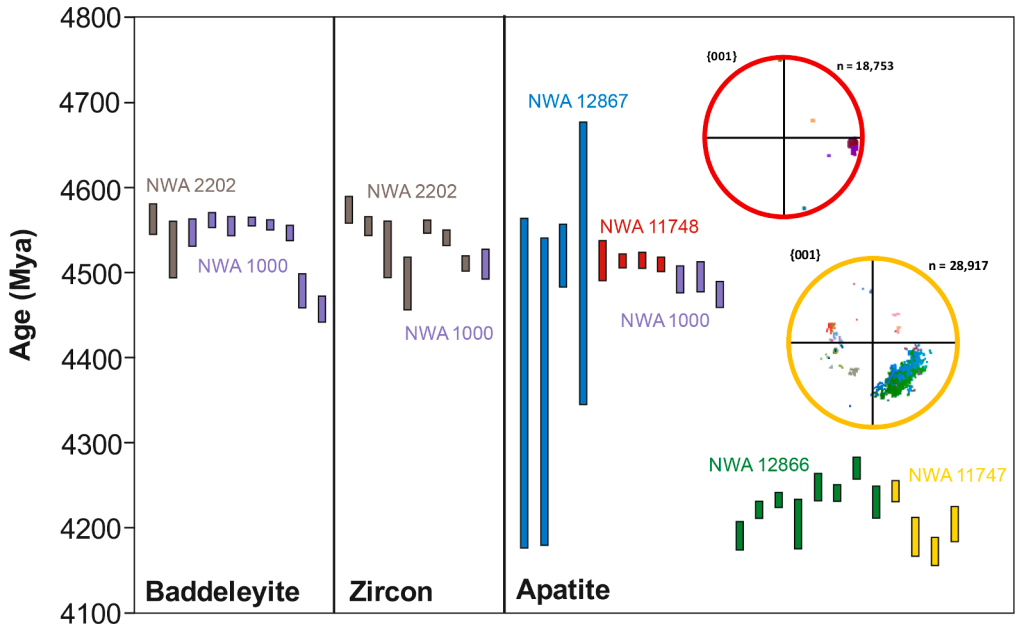

Fig. 6. $^{207}Pb/^{206}Pb$ ages of zircon, baddeleyite, and apatite within all six eucrites analysed in this study (NWA 1000, 2202, 11,747, 11,748, 12,866 and 12,867). For reference, {001} pole figures for apatite in NWA 11,748 (red) and NWA 11,747 (yellow) are shown to highlight the contrast between minimally and intensively plastically deformed apatite (n = number of pixels indexed in EBSD), and the importance of understanding internal crystal structure when accurately interpreting planetary events in the isotope record.

impact deformation or age resetting during the hypothesised late heavy bombardment on the eucrite parent body, suggesting that an uptick in bombardment intensity and the rate was either significantly lower than previously estimated, or did not affect the asteroid 4-Vesta.

CRediT authorship contribution statement

L.F. White: Writing – original draft, Validation, Project administration, Methodology, Investigation, Formal analysis, Data curation, Conceptualization, Writing – review & editing. **D.E. Moser:** Writing – review & editing, Resources, Methodology, Investigation, Funding acquisition, Formal analysis, Data curation, Conceptualization. **J.R. Darling:** Conceptualization, Data curation, Formal analysis, Investigation, Methodology. **B.G. Rider-Stokes:** Data curation, Formal analysis, Investigation, Methodology, Writing – original draft, Writing – review & editing. **B. Hyde:** Investigation, Writing – review & editing. **K.T. Tait:** Resources, Investigation, Funding acquisition, Data curation, Formal analysis. **K. Chamberlain:** Formal analysis, Investigation. **A.K. Schmitt:** Formal analysis, Investigation. **J. Dunlop:** Data curation, Formal analysis, Investigation. **M. Anand:** Validation, Writing – review & editing.

Declaration of competing interest

The authors declare that they have no known competing financial interests or personal relationships that could have appeared to influence the work reported in this paper.

Data availability

Data will be made available on request.

Acknowledgements

This research was supported by an STFC grant to M.A. (grant #ST/T000228/1 and #ST/X001180/1), an NSERC Discovery grant to K. T. T., and a Hatch postdoctoralfellowship to L.F.W. We thank Dr. Yanan Liu (University of Toronto) for assistance with collection of EPMA data used to type meteorites NWA11747, NWA 11748, NWA 12866, and NWA 12867, and we thank Ian Nicklin for discussions around sample selection. We also thank Julia Cartwright and an anonymous reviewer whose comments significantly improved this manuscript, and Frederic Moynier for editorial handling.

Supplementary materials

Supplementary material associated with this article can be found, in the online version, at doi:10.1016/j.epsl.2024.118694.

References

Boehnke, P., Harrison, T.M., 2016. Illusory late heavy bombardments. Proceed. Nat. Acad. Sci. 13 (39), 10802–10806.
Bottke, W., Vokrouhilcky, D., Marchi, S., Swindle, T., Scott, .E.R.D., Weirich, J.R., Levison, H., 2015. Dating the Moon-forming impact event with asteroidal meteorites. Science 348 (6232), 321–323.
Bukovanská, M., Ireland, T.R., Janicke, J., 1997. Zircons and baddeleyites from differentiated meteorites – Basaltic achondrites: ion probe dating and REE systematics. Journal of Geosciences 42 (3), 20.
Cartwright, J.A., Hodges, K.V., Wadhwa, M., 2022. Evidence against a late heavy bombardment event on Vesta. Earth Planet. Sci. Lett. 590, 117576.
Cavosie, A.J., Lugo Centeno, C., 2014. Shocked apatite from the Santa Fe impact structure (USA): a new accessory mineral for studies of shock metamorphism. In: Lunar and Planetary Science Conference, p. 1691.
Cavosie, A.J., Erickson, T.M., Timms, N.E., Reddy, S.M., Talavera, C., Montalvo, S.D., Pincus, M.R., Gibbon, R.J., Moser, D., 2015. A terrestrial perspective on using ex situ shocked zircons to date lunar impacts. Geology 43 (11), 999–1002.
Cavosie, A.J., Timms, N.E., Ferriere, L., Rochette, P., 2018. FRIGN zircon – The only terrestrial mineral diagnostic of high-pressure and high-temperature shock deformation. Geology 46 (10), 891–894.
Cayron, C., Artaud, B., Briottet, L, 2006. Reconstruction of parent grains from EBSD data. Mater Charact 57, 386–401.
Ćernok, A., White, L.F., Darling, J., Dunlop, J., Anand, M., 2019. Shock-induced microtextures in lunar apatite and merrillite. Meteorit. Planet. Sci. 54, 1262–1282.
Chew, D.M., Petrus, J.A., Kamber, B.S, 2014. U–Pb LA–ICPMS dating using accessory mineral standards with variable common Pb. Chem. Geol. 363, 185–199. https://doi.org/10.1016/j.chemgeo.2013.11.006.
Cherniak, D.J. 2010. Diffusion in accessory minerals: zircon, titanite, apatite, mozanite and xenotime. *In: Diffusion in Minerals and Melts,* Zhang, Y., & Cherniak, D. J. Eds.; Reviews in Mineralogy and Geochemistry; Mineralogical Society of America. 72, 827–869.
Cochrone, R., Spikings, R.A., Chew, D., Wotzlaw, J.F., Chiaradia, M., Tyrrell, S., Schaltegger, U., Van der Lelij, R., 2014. High temperature (>350 °C) thermochronology and mechanisms of Pb loss in apatite. Geochemica et Cosmochemica Acta 127, 39–56.
Crow, C.A., McKeegan, K.D., Moser, D.E., 2017. Coordinated U-Pb geochronology, trace element, Ti-in-zircon thermometry and microstructural analysis of Apollo zircons. Geochim. Cosmochim. Acta 202, 264–284.
Darling, J.R., Moser, D.E., Barker, I.R., Tait, K.T., Chamberlain, K.R., Schmitt, A.K., Hyde, B.C., 2016. Variable microstructural response of baddeleyite to shock metamorphism in young basaltic shergottite NWA 5298 and improved U-Pb dating of Solar System events. Earth Planet. Sci. Lett. 444, 1–12.
Darling, J.R., White, L.F., Kizovski, T., Ćernok, A., Moser, D.E., Tait, K.T., Dunlop, J., Langelier, B., Douglas, J.O., Zhao, X., Franchi, I.A., 2020. The shocking state of apatite and merrillite in shergottite NWA 5298 and extreme nanoscale chlorine isotope variability revealed by atom probe tomography. Geochim. Cosmochim. Acta 293, 422–437.
Gattacceca, J., McCubbin, F.M., Bouvier, A., Grossman, J., 2020a. The meteoritical bulletin, No. 107. Meteorit. Planmet. Sci. 55 (2), 460–462.
Gattacceca, J., McCubbin, F.M., Bouvier, A., Grossman, J., 2020b. The meteoritical bulletin, No. 108. Meteorit. Planmet. Sci. 55 (5), 1146–1150.
Grange, M.L., Nemchin, A.A., Pidgeon, R.T., 2013. The effect of 1.9 and 1.4 Ga impact events on 4.3 Ga zircon and phosphate from an Apollo 15 melt breccia. J. Geophys. Res. 118 (10), 2180–2197.
Haba, M.K., Yamaguchi, A., Horie, K., Hidaka, H., 2014. Major and trace elements of zircons from basaltic eucrites: implications for the formation of zircons on the eucrite parent body. Earth Planet. Sci. Lett. 287, 10–21.
Haba, M.K., Wotzlaw, J.F., Lai, Y.J., Yamaguchi, A., Schonbachler, M., 2019. Mesosiderite formation on asteroid 4 Vesta by a hit-and-run collision. Nat Geosci 12 (7), 1–6.
Haba, M.K., Wotzlaw, J.F., 2021. ID-TIMS zircon U-Pb geochronology of the Camel Donga eucrite. Chem. Geol. 567, 120073.
Hannink, R.H.J., Kelly, P.M., Muddle, B.C., 2000. Transformation toughening in zirconia-containing ceramics. J. American Ceramic Soc. 83, 461–487.
Heaman, L.M., 2009. /The application of U-Pb geochronology to mafic, ultramafic and alkaline rocks: an evaluation of three mineral standards. Chem. Geol. 261, 42–51.
Hu, J., Asimow, P., Liu, Y., Ma, C., 2023. Shock-recovered maskelynite indicates low-pressure ejection of shergottites from Mars. Sci Adv 9 (18), eadf2906.
Hublet, G., Debaille, V., Wimpenny, J., Yin, Q.Z., 2017. Differentiation and magmatic activity in Vesta evidenced by ^{26}Al-^{26}Mg dating in eucrites and diogenites. Geochim. Cosmochim. Acta 218, 73–97.
Hughes, J.M., Cameron, M., Crowley, K.D., 1989. Structural variations in natural F, OH, and Cl apatites. American Mineralogist 74, 870–876.
Hopkins, M.D., Mojzsis, S.J., Bottke, W.F., Abramov, O., 2015. Micrometre-scale U-Pb age domains in Eucrite zircons, impact re-setting, and the thermal history of the HED parent body. Icarus 245, 67–378.
Iizuka, T., Yamaguchi, A., Haba, M.K., Amerlin, Y., Holden, P., Zink, S., Huyskens, M.H., Ireland, T.R., 2015. Timing of global metamorphism on Vesta as revealed by high-precision U-Pb dating and trace element chemistry of Eucrite zircon. Earth Planet. Sci. Lett. 409, 182–192.
Iizuka, T., Jourdan, F., Yamaguchi, A., Koefoed, P., Hibiya, Y., Ito, K.T.M., Amelin, Y., 2019. The geological history of Vesta inferred from combined ^{207}Pb/^{206}Pb and ^{40}Ar/^{39}Ar chronology of basaltic eucrites. Geochim. Cosmochim. Acta 267, 275–299.
Jourdan, F., Kennedy, T., Benedix, G.K., Eroglu, E., Mayer, C., 2020. Timing of the magmatic activity and upper crustal cooling of differentiated asteroid 4 Vesta. Geochim. Cosmochim. Acta 273, 205–225.
Jourdan, F., Kennedy, T., Forman, L., Mayers, C., Eroglu, E., Yamaguchi, A., 2024. A slowly cooled deep crust on asteroid 4 Vesta and the recent impact history of rubble pile vestoids recorded by diogenites. Geochim. Cosmochim. Acta 365, 35–52.
Kennedy, T., Jourdan, F., Eroglu, E., Mayers, C., 2019. Bombardment history of asteroid 4 Vesta recorded by brecciated eucrites: large impact event clusters art 4.50 Ga and discreet bombardment until 3.47 Ga. Geochim. Cosmochim. Acta 260, 99–123.
Kenny, G.G., Karlsson, A., Schmieder, M., Whitehouse, M.J., Nemchin, A.A., 2020. Recrystallization and chemical changes in apatite in response to hypervelocity impact. Geology 48 (1), 19–23. https://doi.org/10.1130/G46575.1.
Koike, M., Sano, Y., Takahata, N., Lizuka, T., Ono, H., Mikouchi, T., 2020. Evidence for early asteroidal collisions prior to 4.15 Ga from basaltic eucrite phosphate U-Pb chronology. Earth Planet. Sci. Lett. 549, 11649.
Kring, D.A., Cohen, B.A., 2002. Cataclysmic bombardment throughout the inner solar system 3.9-4.0 Ga. Planets 107 (E2), 4-1.
Kudoh, Y., Takeda, H., Arashi, H., 1986. In situ determination of crystal structure for high pressure phase of ZrO_2 using a diamond anvil and single crystal X-ray diffraction method. Phys Chem Miner 13, 233–237.
Leroux, H., Reimold, W.U., Koerberl, C., Hornemann, U., Doukan, J.C., 1999. Experimental shock deformation in zircon: a transmission electron microscopy study. Earth Planet. Sci. Lett. 44 (3), 390–396.
Lugmair, G.W., Shukolyukov, A., 1998. Early solar system timescales according to ^{53}Mn-^{53}Cr systematics. Geochim. Cosmochim. Acta 62 (16), 2863–2886.
Marchi, S., Bottke, W.F., Cohen, B.A., Wunnemann, K., Kring, D.A., McSween, H.Y., De Sanctis, M.C., O'Brien, D.P., Schenk, P., Raymond, C.A., Russell, C.T, 2013. High-velocaity collisions from the lunar cataclysm recorded in asteroidal meteorites. Nat Geosci 6 (4), 303–307.
McGregor, M., McFarlane, C.R.M., Spray, J.G., 2019. In situ multiphase U-Pb geochronology and shock analysics of apatite, titanite and zircon from the Lac La Moinerie impact structure, Canada. Contribut. Mineral. Petrol. 174, 62.
Misawa, K., Yamaguchi, A., Kaiden, H., 2005. U-Pb and 207Pb-206Pb ages of zircons from basaltic eucrites: implications for early basaltic volcanism on the eucrite parent body. Geochim. Cosmochim. Acta 69 (24), 5847–5861.
Mittlefehldt, D.W., 2015. Asteroid (4) Vesta: I. The howardite-eucrite-digenite (HED) clan of meteorites. Chemie der Erde – Geochemistry 75 (2), 155–183.
Miyamoto, M., Takeda, H., 1977. Evaluation of a crust model of eucrites from the width of exsolved pyroxene. Geochem J 11 (3), 161–169.
Morbidelli, A., Marchi, S., Bottke, W.F., Kring, D.A., 2012. A saw-tooth timeline for the first billion years of lunar bombardment. Earth Planet. Sci. Lett. 355, 144–151.
Morozova, I., 2015. Strength study of zircon under high pressure. *Msc Thesis*. University of Western Ontario (Electronic Thesis and Dissertation Repository, p. 112.
Moser, D.E., Cupelli, C.L., Barker, I.R., Flowers, R.M., Bowman, J.R., Wooden, J., Hart, J. R., 2011. New zircon shock phenomena and their use for dating and reconstruction of large impact structures revealed by electron nanobeam (EBSD, CL, EDS) and isotopic U-Pb and (U-Th)/He analysis of the Vredefort dome. Can J Earth Sci 48 (2), 117–139.
Moser, D.E., Acuri, G.A., Reinhard, D.A., White, L.F., Darling, J.R., Barker, I.R., Larson, D.J., Irving, A.J., McCubbin, F.M., Tait, K.T., Roszjar, J., Wittmann, A.,

Davis, C., 2019. Decline of giant impacts on Mars by 4.48 billion years ago and an early opportunity for habitability. Nat Geosci 12, 522–527.
Nemchin, A.A., Pidgeon, R.T., Healy, D., Grange, M.L., Whitehouse, M.J., Vaughan, J., 2009. The comparative behaviour of apatite-zircon U-Pb systems in Apollo 14 breccias: implications for the thermal history of the Fra Mauro Formation. Meteorit. Planet. Sci. 44 (11), 1717–1734.
Paces, J.B., Miller Jr, J.D, 1993. Precise U-Pb ages of Duluth Complex and related mafic intrusions, northeastern Minnesota: geochronology insights to physical, petrogenic, paleomagnetic, and tectonomagmatic processes associated with the 1.1 Ga Midcontinent Rift system. J. Geophys. Res. 98, 13998–14013.
Pohlner, J.E., Schmitt, A.K., Chamberlain, K.R., Davies, J.H.F.L., Hildenbrand, A., Austermann, G., 2020. Baddeleyite microtextures and U-Pb discordance: insights from the spread eagle intrusive complex and cape St. Mary's sills, Newfoundland, Canada. Geochronology 2 (2), 187–208.
Roszjar, J., Whitehouse, M.J., Srinivasan, G., Mezger, K., Scherer, E.E., Van Orman, J.A., Bischoff, A., 2016. Prolonged magmatism on 4 Vesta inferred from Hf-W analyses of eucrite zircon. Earth Planet. Sci. Lett. 415, 216–226.
Schmedemann, N., Kneissl, T., Ivanov, B.A., Michael, G.G., Wagner, R.J., Neukum, G., Ruesch, O., Hiesinger, H., Krohn, K., Roatsch, T., Preusker, F., Sierks, H., Jaumann, R., Reddy, V., Nathues, A., Walter, S.H.G., Nessemann, A., Raymond, C.A., Russell, C.T., 2014. The cratering record, chronology and surface ages of (4) Vesta in comparison to smaller asteroids and the ages of HED meteorites. Planet Space Sci. 103, 104–130.
Schmieder, M., Moilanen, J., Buchner, E., 2008. Impact melt rocks from the Paasselka impact structure (SE Finland): petrography and geochemistry. Meteorit. Planet. Sci. 43, 1189–1200.
Schmitt, A.K., Chamberlain, K.R., Swapp, S.M., Harrison, T.M., 2010. In situ U-Pb dating of micro-baddeleyite by secondary ion mass spectrometry. Chem. Geol. 269, 386–395.
Schoene, B., Bowring, S.A., 2006. U–Pb systematics of the McClure Mountain syenite: thermochronological constraints on the age of the 40Ar/39Ar standard MMhb. Contribut. Mineral. Petrol. 151, 615.
Schoene, B., Bowring, S.A., 2007. Determining accurate temperature-time paths from U-Pb thermochronology: an example from the Kaapvaal carton, southern Africa. Geochemica et Cosmochimica Acta 71, 165–185.
Schuch, C.S., 2018. Caracterização De Apatitas Da Província Borborema, NE Do Brasil, Como Materiais De Referência Para Geocronologia U-Pb Via LA-ICP-MS. *Monografia (Graduação em Engenharia Geológica)* - Escola de Minas. Universidade Federal de Ouro Preto, Ouro Preto.
Scott, E.R.D., Bogard, D.D., Bottke, W.F., Taylor, G.J., Greenwood, R.C., Franchi, I.A., Keil, K., Moskovitz, N.A., Nesvorny, D., 2009. Impact histories of Vesta and Vestoids inferred from howardites, eucrites and diogenites. In: 40th Lunar and Planetary Science Conference. Houston, Texas.
Smith, D.K., Newkirk, W., 1965. The crystal structure of baddeleyite (monoclinic ZrO_2) and its relation to the polymorphism of ZrO_2. Acta Crystallogr 18, 983–991.
Slaby, E., Forster, H.J., Wirth, R., Wudarska, A., Birski, L., Moszumanska, I., 2017. Validity of the apatite/merrillite relationship in evaluating the water content in the Martian mantle: implications from shergottite Northwest Africa (NWA) 2975. Geosciences (Basel) 7 (4), 99.
Takenouchi, A.H., Sumino, T., Mikouchi, T., Ono, H., Yamaguchi, A., 2021. Argon-Argon chronology of two shocked eucrites, Northwest Africa 1000 and Yamato 980433. In: 52nd Lunar and Planetary Science Conference, p. 1742.
Tera, F., Papanastassiou, D.A., Wasserburg, G.J., 1974. Isotopic evidence for a terminal lunar cataclysm. Earth Planet. Sci. Lett. 22 (1), 1–21.
Thomson, S.N., Gehrels, G.E., Ruiz, J., Buchwaldt, R., 2012. Routine low-damage apatite U-Pb dating using laser ablation Multicollector ICPMS, 13. Geochemistry, Geophysics, Geosystems.
Timms, N.E., Erickson, T.M., Pearce, M.A., Cavosie, A.J., Schmieder, M., Tohver, E., Reddy, S.M., Zanetti, M.R., Nemchin, A.A., Wittmann, A., 2017. A pressure-temperature phase diagram for zircon at extreme conditions. Earth-Sci. Rev. 165, 185–202.
Touboul, M., Sprung, P., Aciego, S.M., Bourdon, B., Kleine, T., 2015. Hf-W chronology of the Eucrite parent body. Geochim. Cosmochim. Acta 156, 106–121.
Warren, P.H., 2002. Northwest Africa 1000: A new Eucrite with Maskelynite, Unequilibrated pyroxene crisscrossed by Fayalite-rich veins, and Stannern-like geochemistry. Lunar and Planetary Science XXXIII, p. 1147 abstract.
Wetherill, G.W., 1975. Late heavy bombardment of the moon and terrestrial planets. In: In: Lunar Science Conference, 6th. Houston, 6, pp. 1539–1561. *Texas*.
White, L.F., Darling, J.R., Moser, D.E., Reinhard, D.A., Prosa, T.J., Bullen, D., Olson, D., Larson, D.J., Lawrence, D., Martin, I., 2017. Atomic-scale age resolution of planetary events. Nat Commun 8, 15597.
White, L.F., Darling, J.R., Moser, D.E., Cayron, C., Barker, I., Dunlop, J., Tait, K.T., 2018. Baddeleyite as a widespread and sensitive indicator of meteorite bombardment in planetary crusts. Geology 46 (8), 719–722.
White, L.F., Moser, D.E., Tait, K.T., Langelier, B., Barker, I., Darling, J.R., 2019. Crystallization and impact history of a meteoritic sample of early lunar crust (NWA 3163) refined by atom probe geochronology. Geosci. Front. 10 (5), 1841–1848.
White, L.F., Ćernok, A., Darling, J.R., Whitehouse, M.J., Joy, K., Cayron, C., Dunlop, J.N., Tait, K.T., Anand, M., 2020. Evidence of extensive lunar crust formation in impact melt sheets 4,330Myr ago. Nature Astronomy 4, 974–978.
Yamaguchi, A., Taylor, G.J., Keil, K., 1996. Global crustal metamorphism of the eucrite parent body. Icarus 124, 97–112.
Yamaguchi, A., Barrat, J.A., Greenwood, R.C., Shirai, N., Okamoto, C., Setoyanagi, T., Ebihara, M., Franchi, I.A., Bohn, M., 2009. Crustal partial melting on Vesta: evidence from highly metamorphosed eucrites. Geochim. Cosmochim. Acta 73 (23), 7162–7182.
Zhou, Q., Yin, Q.Z., Young, E.D., Li, X.H., Wu, F.Y., Li, Q.L., Liu, Y., Tang, G.Q., 2013. SIMS Pb-Pb and U-Pb age determination of eucrite zircons at $< 5\mu m$ scale and the first 50 Ma of the thermal history of Vesta. Geochim. Cosmochim. Acta 110, 152–175.